

Journal of Materials Chemistry C

Accepted Manuscript



This is an *Accepted Manuscript*, which has been through the Royal Society of Chemistry peer review process and has been accepted for publication.

Accepted Manuscripts are published online shortly after acceptance, before technical editing, formatting and proof reading. Using this free service, authors can make their results available to the community, in citable form, before we publish the edited article. We will replace this *Accepted Manuscript* with the edited and formatted *Advance Article* as soon as it is available.

You can find more information about *Accepted Manuscripts* in the [Information for Authors](#).

Please note that technical editing may introduce minor changes to the text and/or graphics, which may alter content. The journal's standard [Terms & Conditions](#) and the [Ethical guidelines](#) still apply. In no event shall the Royal Society of Chemistry be held responsible for any errors or omissions in this *Accepted Manuscript* or any consequences arising from the use of any information it contains.

Modelling the Luminescence of Extended Solids: the example of a Highly Luminescent MCM-41 Impregnated with a Eu^{3+} β -diketonate complex

Mario R. Felício^a, Teresa G. Nunes^b, Patrícia M. Vaz^c, A. M. P. Botas^{d,e}, Paulo Ribeiro-Claro^c, Rute A.S. Ferreira^d, Ricardo O. Freire^f, Pedro D. Vaz^g, Luís D. Carlos^d, Carla D. Nunes^{a*}, Mariela M. Nolasco^{d*}

^a Centro de Química e Bioquímica, Departamento de Química e Bioquímica, Faculdade de Ciências da Universidade de Lisboa, 1749-016 Lisboa, Portugal

^b Centro de Química Estrutural, Instituto Superior Técnico, Av. Rovisco Pais, 1049-001 Lisboa, Portugal

^c Chemistry Department and CICECO, University of Aveiro, 3810-193 Aveiro, Portugal

^d Physics Department and CICECO, University of Aveiro, 3810-193 Aveiro, Portugal

^e I3N, University of Aveiro, Aveiro, Portugal

^f Pople Computational Chemistry Laboratory, Departamento de Química, Universidade Federal de Sergipe, 49.100-000 – São Cristóvão, SE, Brazil

^g Pedro D Vaz, ISIS Pulsed Neutron & Muon Facility, Rutherford Appleton Laboratory, Chilton Didcot, Oxon, OX11 0QX, United Kingdom

E-mail: mnolasco@ua.pt; cmnunes@fc.ul.pt

* Correspondence to: Dr. Mariela M. Nolasco, Physics Department and CICECO, University of Aveiro, 3810-193 Aveiro, Portugal, Dr. Carla D. Nunes, Centro de Química e Bioquímica, Departamento de Química e Bioquímica, Faculdade de Ciências da Universidade de Lisboa; 1749-016, Lisboa, Portugal

Abstract

The regular MCM-41 type mesostructured silica material was used as a support for the incorporation of the highly luminescent tris(β -diketonate) complex $\text{Eu}(\text{tta})_3\text{phen}$ yielding the hybrid MCM-Eu material. Suitable characterization by powder X-ray diffraction (XRD), thermogravimetric analyses (TGA), diffuse reflectance infrared Fourier transform spectroscopy (DRIFTS), ^{13}C and ^{21}Si solid state NMR spectroscopy and photoluminescence spectroscopy was accomplished. The combination of Ultraviolet-Visible spectroscopy (UV-Vis) and photoluminescence techniques shows that this incorporation seems to modify essentially the second Eu^{3+} coordination shell. For a material that has a simply impregnated lanthanide complex, the herein reported maximum $^5\text{D}_0$ quantum yield (q) value of 0.31 is a significant high value, being almost in the same scale of the values obtained for the materials with covalently bonded complexes. A detailed theoretical photoluminescence study of the MCM-Eu with the recently developed Luminescence Package- LUMPAC is presented. The high accuracy of the theoretical calculations is achieved through the comparison with the experimental values. Aiming at a deeper understanding of the photoluminescence process, the ligand-to- Eu^{3+} intramolecular energy transfer and back-transfer rates were also predicted. The dominant pathway involves the energy transfer between the lowest energy ligand triplet and the $^5\text{D}_0$ level ($9.70 \times 10^7 \text{ s}^{-1}$).

Keywords

- β -diketonate
- Europium
- MCM-41
- LUMPAC
- Energy transfer

1. Introduction

The unique optical properties of luminescent lanthanide (Ln^{3+}) complexes to emit well-defined narrow bands in different spectral ranges with relatively long lifetimes and high quantum yields makes them appropriate for technological applications¹⁻⁴. The interest in these materials has progressively grown in the last two decades due to their wide range of potential photonic applications such as amplifiers for optical communications,⁵ components of the emitter layers in multilayer organic light-emitting diodes (OLEDs),⁶ tunable lasers,⁷ luminescent labels in advanced time-resolved fluoroimmunoassays,⁸ light concentrators for photovoltaic devices,⁹ luminescent thermometers¹⁰ and magnetic resonance imaging (MRI) contrast agents¹¹. The design of new organic photosensitizers has dominated the development of Ln^{3+} -based optical materials in view of their high molar absorption coefficients and their efficient sensitization ability of the metal-centered luminescence. Although a large number of anionic ligands have been developed and tested for their ability to sensitize Ln^{3+} luminescence, β -diketones appear to be adequate sensitizers to meet the requirements^{12,13}. Up to date, the experimental quantum yield measured for $\text{Eu}(\text{tta})_3\text{ephen}$ [tta^- = 2-thenoyltrifluoroacetate; ephen = 5,6-epoxy-5,6-dihydro-(1,10)phenanthroline], $82\pm 8\%$, is one of the highest so far reported for solid-state europium complexes¹⁴.

The rather low thermal and photochemical stability together with poor mechanical properties and photodegradation upon UV exposure represent important disadvantages concerning the technological applicability of the Ln^{3+} β -diketonate complexes. Their incorporation in polymers^{15,16}, liquid crystals¹⁷, organic-inorganic hybrid materials^{14,18-24}, Zeolite L²⁵, mesoporous materials^{26,27}, silica nanoparticles^{28,29} and multi-walled carbon nanotubes³⁰ overcomes these drawbacks and provide Ln^{3+} -containing hybrid materials with high potential for different applications^{4,19,23,24,31}.

Due to its peculiar characteristics, large internal surface area and favourable uniformity and easily controlled size of the pore, the regular MCM-41 type mesostructured silica material has attracted considerable interest in physics, chemistry, materials science and other relevant areas. These properties together with the thermal and mechanical stabilities make it an ideal host for incorporation of active/functional molecules and some work has already been devoted on this field

³²⁻³⁶. Several procedures have been extensively explored in the last few years to immobilize lanthanide complexes in MCM-41³⁷⁻³⁹. The most straightforward method that can be employed to encapsulate lanthanide ions in MCM-41 or MCM-48 supports involves simple embedding of the complex⁴⁰⁻⁴⁶ within prefunctionalized or as-prepared mesoporous silica networks by means of simple wet impregnation methods.

In the last few years the use of theoretical models to determine the coordination geometry of a lanthanide complex⁴⁷⁻⁴⁹, the position and nature of the ligand excited states in the complex⁴⁷⁻⁴⁹, the 4f–4f intensity parameters^{50,51}, the ligand-to-lanthanide ion energy transfer rates⁵⁰⁻⁵², and the luminescence quantum yields⁵³ was very restricted. The main reason was the fact that these models are a somewhat difficult to apply and also because until now no software with the models for the luminescence properties calculations implemented had been developed. With the goal to contribute to the diffusion and use of theoretical methods to understanding and designing lanthanide-based luminescent systems, the easy-to-use computational package LUMPAC⁵⁴ was recently developed. In order to gain insight into the factors which determine the quantum yield and other relevant properties of lanthanide complexes, our group has adopted the LUMPAC's approach based on both theoretical and experimental work and therefore will be herein used to theoretically support the photoluminescence studies. The reported methodology offers an opportunity to calculate the photoluminescence properties of luminescent materials, being simple and precise enough to predict the emission quantum yields of hybrid materials. In fact, the suitability of the LUMPAC's approach for modelling the photoluminescence properties of extended solids such as Metal-Organic Frameworks was recently assessed⁵⁵. The incorporation of luminescent lanthanide materials in solid matrices with structural organization is of widespread interest in materials since as it affords functional materials with a variety of optical properties. Compared with the lanthanide complex, the MCM-based material provides an additional advantage, such as being able to be processed as silica-based templates for optical centres (compatible with the silicon devices technology), opening up the possibility of designing new luminescent displays with highly oriented MCM-41 films impregnated

with enhanced emitting centres. Therefore, in this paper, the incorporation of $\text{Eu}(\text{tta})_3\text{ephen}$ into MCM-41 by impregnation method is described and the structure and photoluminescence features of a novel highly luminescent mesoporous material incorporating the $\text{Eu}(\text{tta})_3\text{ephen}$ complex is investigated and theoretically explored.

2. Experimental

2.1 Synthetic procedures

All reagents were obtained from Aldrich and used as received. Commercial grade solvents were dried and deoxygenated by standard procedures (CH_2Cl_2 over CaH_2), distilled under nitrogen, and kept over 4 Å molecular sieves. $\text{Eu}(\text{tta})_3\text{ephen}$ was prepared and characterized according to the literature¹⁴. MCM-41 was synthesized by adopting a methodology previously described, using $[(\text{C}_{14}\text{H}_{33})\text{N}(\text{CH}_3)_3]\text{Br}$ as template⁴⁶. Template extraction from MCM-41 was performed by refluxing the materials with HCl acidified methanol instead of a calcination procedure⁵⁶. Prior to the grafting experiment, physisorbed water and methanol were removed by heating at 453 K in vacuum (10^{-2} Pa) for 2 h. A suspension of MCM (0.290 g) in dichloromethane reacts with a solution of $\text{Eu}(\text{tta})_3\text{ephen}$ (0.081 g) in dichloromethane. The mixture was stirred overnight under N_2 inert atmosphere, then filtered, washed with 2 x 10 mL of dichloromethane, and dried under vacuum during 3 h, to yield **MCM-Eu**. Elemental analysis (%): found C 4.70, S 1.06, N 0.31, H < 0.5.

2.2 Characterization

Solid state ^{29}Si and ^{13}C NMR measurements were performed at room temperature on a Bruker MSL 300P spectrometer operating at 59.60 and 75.47 MHz for the observation of ^{29}Si and ^{13}C resonances, respectively. The standard magic angle spinning (MAS) cross polarization – dipolar decoupling RF pulse sequence (CP-DD) was used under about 4 kHz spinning rate. For the acquisition of ^{29}Si spectra, 5 ms contact time was chosen, 6 s recycling delay, and a number of scans always higher than 3000 were selected; the Hartmann-Hahn condition was optimized using tetrakis-trimethylsilylsilane and tetramethylsilane (TMS) was the external reference to set the

chemical shift scale. ^{13}C spectra were recorded with 2 ms contact time, 4 s recycling delay and a number of scans higher than 900. The Hartmann-Hahn condition was optimized using glycine, also the external reference to set the chemical shift scale (^{13}CO at 176.1 ppm).

Powder X-ray diffraction (XRD) measurements were taken on a Philips Analytical PW 3050/60 X'Pert PRO (theta/2 theta) equipped with X'Celerator detector and with automatic data acquisition (X'Pert Data Collector (v2.0b) software), using a monochromatized Cu-K α radiation as incident beam, 40 kV–30 mA. Thermogravimetric analyses (TGA) were performed using a Perkin-Elmer TGA7 thermobalance system at a heating rate of 10 K min $^{-1}$ under N $_2$ between 300 and 1073 K. Microanalyses were performed at the Elemental Analysis Service of IST. DRIFT spectra were acquired with a MATTSON 7000 FTIR Spectrometer fitted with Spectra-Tech diffuse reflectance (diffuse reflectance infrared Fourier transform-DRIFT) accessory. Spectra were measured in the 400-4000 cm $^{-1}$ range using 2 cm $^{-1}$ resolution. The Ultraviolet-Visible (UV-Vis) absorption spectra of the ethanolic solutions were measured at room temperature on a JASCO V-560 instrument with a scan range of 220-850 nm, at 200 nm min $^{-1}$ and a resolution of 0.5 nm.

The photoluminescence spectra were recorded at room temperature and at 12K with a modular double grating excitation spectrofluorimeter with a TRIAX 320 emission monochromator (Fluorolog-3, Horiba Scientific) coupled to a R928 Hamamatsu photomultiplier, using a front face acquisition mode. The excitation source was a 450 W Xe arc lamp. The emission spectra were corrected for detection and optical spectral response of the spectrofluorimeter and the excitation spectra were corrected for the spectral distribution of the lamp intensity using a photodiode reference detector. The emission monochromator has a linear spectral density of 2.64 nm.mm $^{-1}$ and the slits width was 0.03 nm, yielding a spectral resolution around 2.3 cm $^{-1}$.

The absolute emission quantum yields (q) were measured at room temperature using a quantum yield measurement system C9920-02 from Hamamatsu with a 150 W Xenon lamp coupled to a monochromator for wavelength discrimination, an integrating sphere as sample chamber and a

multi channel analyser for signal detection. Three measurements were made for each sample so that the average value is reported. The method is accurate to within 10 %.

2.3 Theoretical calculations

The hybrid MCM-Eu system's ground state geometry was based on a $\text{Eu}(\text{tta})_3\text{ephen}$ complex molecule impregnated in a truncated MCM-41 pore. The 3D hexagonal structure model of an MCM-41 channel was built using an online application⁵⁷. The model channel obtained in this way has all silanol groups in the wall's outer surface. They were then inverted to the inner surface wall using Moldraw software⁵⁸. This was accomplished by aligning a single side of the hexagon along the xy plane and then mathematically inverting the signal of the negative sign of all the OH groups on that surface. The procedure was replicated five more times by rotating the channel 60° prior to it. This allowed all hydroxyl groups to lie on the inner surface of the channel. All silicon atoms saturated by oxygen atoms and oxygen atoms with less than two silicon atoms attached to them are saturated by hydrogen atoms. The model channel was optimized with the UFF molecular mechanics method available in the Gaussian 03W - Revision D.02 program package⁵⁹.

Due to the large size of the hybrid system (708 atoms) the geometry optimization was performed with the semiempirical Sparkle model⁶⁰⁻⁶⁴ implemented in MOPAC2012⁶⁵. The choice of which Sparkle model to be used is related with the impact of AM1 (Austin Model 1), PM3 (Parametric Method 3), PM6 (Parametric Method 6), RM1 (Recife Model 1) or PM7 (Parametric Method 7), on the quantum chemical modelling of the specific atoms of the system under study. The optimization of the ground state geometry by the Sparkle/AM1 model allows accurate geometry prediction as *ab initio*/ECP (effective core potential) calculations on lanthanide complexes, while being hundreds of time faster^{60,66}. Additionally, as it was successfully applied in Eu^{3+} -based organic-inorganic hybrids⁶⁷, we decide to perform Sparkle/AM1⁶⁰ calculations. The keywords used were: AM1; SPARKLE; PRECISE; GNORM=0.25; T=10D; GEO-OK and XYZ: The singlet and triplet excited states energies were performed by using the semiempirical INDO/S-CIS^{68,69} (Intermediate Neglect of Differential Overlap/Spectroscopic - Configuration Interaction Single) implemented in ORCA⁷⁰.

The luminescent properties: intensity parameters, radiative and non-radiative rates, energy transfer and back-transfer rates, quantum efficiency and quantum yield were calculated using the LUMPAC software⁵⁴. The methodologies implemented in LUMPAC to calculate these luminescent properties are detailed in reference⁷¹ and in the LUMPAC's homepage (<http://www.lumpac.pro.br/theory>).

3. Results and discussion

The MCM-41 material was prepared using myristyltrimethylammonium bromide ($[(C_{14}H_{33})N(CH_3)_3]Br$) as surfactant, according to a literature procedure⁴⁶. Afterward, the $Eu(tta)_3$ phen complex (Scheme 1) was impregnated on the inner surface of the material. The Eu complex was introduced by suspending the MCM material in dichloromethane and then adding the precursor complex as a dichloromethane solution. This afforded MCM-Eu material, and according to elemental analysis, the CHN analyses for **MCM-Eu** material revealed values of 4.7 %C, 0.31 %N, 1.06 %S, and %H < 0.5. Based on the *N* and *S* content, these results show that the loading of $Eu(tta)_3$ phen derivative inside the pores is 0.11 mmol g⁻¹. The material was conveniently characterized by DRIFT, powder XRD, TGA and ²⁹Si and ¹³C CP-MAS SS/NMR. All spectroscopic features discussed in the following lines were found to be in agreement with related mesoporous materials.

[Scheme 1]

3.1 Synthesis and characterization

The powder XRD patterns of MCM and MCM-Eu are given in Figure 1. The pattern of the parent, calcined MCM material, shows four reflections in the $2^\circ < 2\theta < 10^\circ$ range, indexed to a hexagonal cell as (100), (110), (200), and (210). The *d* value of the (100) reflection is 38.3 Å, corresponding to a lattice constant of $a = 44.3 \text{ \AA} (= 2d_{100}/\sqrt{3})$. For material MCM-Eu the *d* value of the (100) reflection is 37.7 Å, corresponding to a lattice constant of $a = 44.3 \text{ \AA} (= 2d_{100}/\sqrt{3})$.

[Figure 1]

After the inclusion of the $\text{Eu}(\text{tta})_3\text{ephen}$ complex, the characteristic reflections are still observed at about the same positions, demonstrating that the long-range hexagonal symmetry of the mesoporous host was preserved. The observed peak intensity reduction is common to materials containing guest species. This is not due to a crystallinity loss, but rather to an X-ray scattering contrast reduction between the silica walls and pore-filling material. This has been observed for other types of materials and is well described in the literature⁷²⁻⁷⁴.

[Figure 2]

Figure 2 shows the thermogravimetric analyses (TGA) of materials (host and composite) discussed in the present work. Both materials show mass losses till 400 K corresponding to physisorbed water. For the MCM parent material, after the plateau between 400 and 550 K, there is further mass loss due to water molecules involved in stronger interactions with the host matrix up until ca. 700 K. After this temperature mass loss is mostly due to dehydroxylation of surface silanol groups. On the other hand, TGA analysis of MCM-Eu shows a degradation step occurring between 400–1073 K with a loss of 10.70% due to the presence of the Eu complex inside the pores of the host material. This weight loss corresponds to a loading of 0.11 mmol g^{-1} (0.011 mol %) of the complex inside the MCM pores. This loading matches exactly the value determined by elemental analysis based on the *N* and *S* contents, as discussed earlier in this work.

The materials were also characterized by ^{29}Si CP MAS-DD solid state NMR. The ^{29}Si CP MAS-DD NMR spectrum of pristine MCM, displays three resonances at -109.7, -100.5 and -91.8 ppm, characteristic of Q^4 , Q^3 and Q^2 species of the silica framework, respectively (Fig. 3). For material MCM-Eu three resonances were also observed at -110.1, -100.8 and -91.5 ppm, characteristic of Q^4 , Q^3 and Q^2 species.

[Figure 3]

The DRIFT spectra ($850\text{-}1750 \text{ cm}^{-1}$) of the $\text{Eu}(\text{tta})_3\text{ephen}$, MCM and MCM-Eu are presented in Fig. 4 (the complete DRIFT are depicted in Figure S1 of the SI). The DRIFT spectrum of the MCM host

material is typical of a silicate evidencing a broad band in the 3600-2600 cm^{-1} range due to hydrogen bonding silanol groups (Figure S1, SI). Other important features comprise the band at ca. 1640 cm^{-1} due to δOH bending modes while the intense broad band at 900-1260 cm^{-1} is assigned to the asymmetric stretching vibration modes of the mesoporous framework ($\nu\text{Si-O-Si}$)⁷⁵. After the $\text{Eu}(\text{tta})_3\text{ephen}$ incorporation, the DRIFT spectrum shows an overall similar profile dominated by the strong and broad bands of the host MCM material and most of the bands due to $\text{Eu}(\text{tta})_3\text{ephen}$ are not evident. However, new bands (highlighted in Fig.4, red line) were detected evidencing the $\text{Eu}(\text{tta})_3\text{ephen}$ presence within the pores.

[Figure 4]

Figure 5 shows the normalised UV-Vis absorption spectra of $\text{Eu}(\text{tta})_3\text{ephen}$ and the **MCM-Eu** sample in ethanol solutions. The electronic absorption spectrum of complex $\text{Eu}(\text{tta})_3\text{ephen}$ shows five broad bands with maxima at 267, 288, 299, 309 and 340 nm arising from the sum of the tta and ephen ligands¹⁴. On the basis of the molecular orbitals involved in the dominant excitation of each absorption, the observed bands at 288, 309 and 340 nm (with correspondence with the calculated ones at 276, 290, 324 nm) are assigned to excitations predominantly involving singlet intraligand (^1IL) $\pi \rightarrow \pi^*_{\text{tta}}$ transitions although with some minor contributions from the ephen ligand. In turn, the bands at 267 and 299 nm (with correspondence with the calculated ones at 234 and 286 nm) receive a great contribution of the ^1IL $\pi \rightarrow \pi^*_{\text{ephen}}$ transitions¹⁴. Comparing the absorption spectrum of the MCM-Eu sample with that of $\text{Eu}(\text{tta})_3\text{ephen}$ obvious differences in the absorption bands attributed to both tta and ephen ligands are observed. The corresponding red shift (340 \rightarrow 344 nm) is observed, suggesting that the electron distribution of the conjugated system involving the tta chelated ring changed when the $\text{Eu}(\text{tta})_3\text{ephen}$ was incorporated into the MCM-41 matrix. Additionally, a significant intensity increase is observed for the bands with maxima at 288, 299 and 309 nm, suggesting that both tta and ephen ligands are slightly affected with the incorporation of $\text{Eu}(\text{tta})_3\text{ephen}$ within the constrained environment of the channels of the MCM-41 matrices. As these results demonstrate the integrity of the first-sphere ligands in the hybrid material, the

structural changes are expected to occur outside the coordination polyhedron, modifying essentially the second Eu^{3+} coordination shell, most likely by the establishment of intermolecular interactions. The same conclusion has already been observed for the hybrid system based on the $\text{Eu}(\text{tta})_3\text{ephen}$ complex and the tri-ureasil matrix¹⁴ as well as for an analogous hybrid system based on the $\text{Eu}(\text{tta})_3\text{phen}$ (phen = 1,10-phenanthroline) and the poly(ϵ -caprolactone)siloxane organic-inorganic biohybrid⁷⁶.

[Figure 5]

3.2 Photoluminescence studies

The **MCM-Eu** sample displays room-temperature emission ascribed to the $\text{Eu}^{3+} \ ^5\text{D}_0 \rightarrow \ ^7\text{F}_{0-4}$ transitions, Figure 6. The excitation paths for the intra-4f⁶ emission can be visualised in the excitation spectra monitored around the $\ ^5\text{D}_0 \rightarrow \ ^7\text{F}_2$ transition (Figure 6). The spectrum is formed of a broad band (240-420 nm) peaking at ~ 375 nm. The high- and low-wavelength regions were recently ascribed to the preferential excitation of the ephen and tta excited states, respectively¹⁴. The presence of a very-low intense Eu^{3+} transition ($\ ^7\text{F}_0 \rightarrow \ ^5\text{D}_2$) readily indicates that the Eu^{3+} ions are mainly sensitized by the ligands, rather than by direct intra-4f⁶ excitation. The maximum quantum yield value (q) (0.31 ± 0.03) was found under excitation at 320 nm. Similar values (within the experimental error) were measured under excitation at 275 and 375 nm (0.26 ± 0.03).

[Figure 6]

For a material that has a simply impregnated lanthanide complex, the herein reported maximum η value of 0.31 is a very significant value. In fact, it's higher than those reported for lanthanide complexes that are immobilized in the host with weak interactions or with pre-functionalized matrix^{44,76}, being almost in the same scale of those values obtained for the materials with covalently bonded complexes.^{37-39,77,78}

Aiming at further discussing the Eu^{3+} -local environment, Figure 7a displays the intra-4f⁶ transitions scanned with higher resolution at 10 K under distinct excitation wavelengths. The emission spectra

are independent of the excitation wavelength in good agreement with the presence of a single average Eu^{3+} -local environment. Moreover, the non-degenerated ${}^5\text{D}_0 \rightarrow {}^7\text{F}_0$ transition is well described by a single Gaussian a function (Figures 7b and c) peaking at $17252.5 \pm 0.3 \text{ cm}^{-1}$ with a full-width-at-half-maximum (fwhm) of $24.7 \pm 0.2 \text{ cm}^{-1}$. Furthermore, the fact that the ${}^7\text{F}_{1,2}$ levels split into 3 and 5 Stark components (marked with arrows in Figure 7a) and the higher intensity of the ${}^5\text{D}_0 \rightarrow {}^7\text{F}_2$ transition point out that the Eu^{3+} ions in the occupy the same average local environment characterized by a low-symmetry group without an inversion centre. We should note that the values of the energy and fwhm of ${}^5\text{D}_0 \rightarrow {}^7\text{F}_0$ transition are higher than those previously reported for the isolated complex ($17249.0 \pm 0.1 \text{ cm}^{-1}$, fwhm of $13.7 \pm 0.2 \text{ cm}^{-1}$) as also observed for the same complex incorporated into the tri-ureasil host¹⁴. The larger fwhm, often termed as inhomogeneous broadening induced site-to-site variation reflects the complex accommodation into the host materials.

[Figure 7]

The ${}^5\text{D}_0$ lifetime value was measured under excitation at 275 and 375 nm (Figure S2, SI) through the monitoring of the emission decay curves around the ${}^5\text{D}_0 \rightarrow {}^7\text{F}_2$ transition. Both curves are well described by a single exponential function (Figure S2, SI), in good agreement with the presence of a single Eu^{3+} -local environment yielding lifetime values of 0.635 ± 0.001 (275 nm) and 0.671 ± 0.001 (375 nm). Although smaller than those measured for the complex (0.896 ± 0.004 , excited at 270 nm insert value) and after incorporation into the tri-ureasil host¹⁴, (0.750 ± 0.003 , excited at 270 nm), the ${}^5\text{D}_0$ lifetime dependence with the excitation wavelength was also observed for the same complex and indicates that ligand-to- Eu^{3+} energy transfer processes are operative and mediated by an intermediate state (such as the triplet states of the ligands) in near-resonance with the intra- $4f^6$ levels⁷⁹.

All these aspects, in particular the transitions broadening and lifetime decrease seem to indicate that impregnation of the complex into the channels of the MCM-41 matrices modifies essentially the

second Eu^{3+} coordination shell. The transitions broadening is in accordance with a higher non-homogeneous distribution of similar Eu^{3+} chemical environments due to changes outside the coordination polyhedron, essentially related with the amorphous local structure of the host that accommodates in slightly different ways the Eu^{3+} first-coordination sphere (and also leading to slight modifications in the phonon density distribution)⁸⁰.

Aiming at a further theoretical rationalization of the photoluminescence properties, the experimental $^5\text{D}_0$ radiative (k_r) and non-radiative (k_{nr}) transition probabilities and the $^5\text{D}_0$ quantum efficiency (η), $\eta = k_r / (k_r + k_{nr})$ were also estimated and compared with the theoretical values (discussed hereinafter). The procedure to estimate these values was based on the $^5\text{D}_0 \rightarrow ^7\text{F}_{0-4}$ integrated areas and $^5\text{D}_0$ lifetime, recorded at room temperature for the same excitation wavelength of 375 nm¹⁹. The experimental intensity parameters Ω_2 and Ω_4 were determined from the emission spectra of Figure 7a(2) using the $^5\text{D}_0 \rightarrow ^7\text{F}_2$ and $^5\text{D}_0 \rightarrow ^7\text{F}_4$ transitions, respectively. The Ω_6 parameter was not determined since the $^5\text{D}_0 \rightarrow ^7\text{F}_6$ transition is not observed experimentally. The obtained Ω_2 , Ω_4 , k_r , k_{nr} and η values are displayed in Table 1.

[Table 1]

3.3 Theoretical rationalization of the photoluminescence properties.

Owing to the recent development of the Luminescence Package- LUMPAC⁵⁴, it was decided to carry out a study to assess whether this software, freely available to the scientific community, could be used with confidence to theoretically rationalize the photoluminescence properties of the hybrid **MCM-Eu** material. As such, a report on the feasibility of using LUMPAC calculations is presented by comparing the obtained theoretical values with the experimental ones.

The molecular structure determination is the first step in the rationalization and prediction of the luminescent properties. In fact, from the optimized geometry, we can proceed to calculate many photoluminescent properties such as: singlet and triplet energy states, intensity parameters, radiative and nonradiative rates, energy transfer and back-transfer rates, quantum efficiency and quantum

yied. However, the recognition of the molecular model to be used must be done in a way to justify the experimental results as a whole. It should be take into account that organized media can significantly influence the photophysical processes on guest molecules. These hosts are able to provide a variety of different microchemical environments for the guest molecule, ultimating the occurrence of intermolecular interactions with the host⁸¹. UV-Vis results together with the photoluminescence data led to a picture where the impregnation of the complex into the channels of the MCM-41 matrices modifies essentially the second Eu³⁺ coordination shell, most likely by the establishment of intermolecular interactions. These spectroscopic results gave us confidence to build a molecular model to contemplate such interactions. For that reason, one of the possible MCM-Eu system's ground state geometry, based on a Eu(tta)₃ephen complex molecule impregnated in a truncated MCM-41 pore (for further details see Section 2.3), evidencing the presence of C-H...O intermolecular interactions between C-H groups of both tta an ephen ligands and the silanol oxygen from the MCM-41 host, is shown in Figure 8. The complete optimization was achieved with the Sparkle/AM1 model and performed in module 1 of LUMPAC. It should be emphasized that, due to the good agreement between the experimental and theoretical results (discussed hereinafter) this simplified model efficiently represents the real system with respect to the electronic properties.

[Figure 8]

The optimized coordinates of the MCM-Eu system were used as input data to calculate the singlet (S₁) and triplet (T₁) energy levels as well as the theoretical intensity parameters Ω_2 , Ω_4 and Ω_6 of the Eu(tta)₃ephen coordination polyhedron. The theoretical intensity parameters (Table 1) were obtained from a set of values of charge factors (g) and polarizabilities (α) associated with each europium-atom-ligand bond (Table 2) that were adjusted to reproduce the experimental intensity parameters Ω_2 and Ω_4 .

[Table 2]

These calculations were performed, respectively, in modules 2 and 3 of LUMPAC. The obtained Ω_2 , Ω_4 and Ω_6 values are listed in Table 1 and the S_1 and T_1 energies are 33742 cm^{-1} and 18985 cm^{-1} , respectively. It should be noted that although the lowest triplet state (18985 cm^{-1}) lies below the acceptor level 5D_1 of the Eu^{3+} ion⁸², an efficient ligand-to-metal energy transfer is possible. In fact, there are some reports on the literature related with europium complexes with T_1 energy levels between 5D_1 (19027 cm^{-1})⁸² and the 5D_0 emitting level (17293 cm^{-1})⁸², with highly efficient energy transfer rates⁸³⁻⁸⁸.

These theoretical parameters were used to calculate the theoretical 5D_0 radiative (k_r) and non-radiative (k_{nr}) transition probabilities, as well as the 5D_0 emission quantum efficiency (η) and quantum yield (q) values. The comparison between all the calculated theoretical values and the experimental ones can be found in Table 1.

The theoretical and experimental values are in very good agreement which allow us to assert that the LUMPAC calculations are able to support photoluminescence studies in extended solids in a very accurately way, provided the appropriate molecular model. The very low value calculated for the Ω_6 parameter is also in good agreement with the negligible intensity of the $^5D_0 \rightarrow ^7F_6$ transition.

The values of charge factors (g) and the ligating ion polarizability (α) were adjusted using a non-linear minimization of a six-dimension response surface. The Generate Simulating Annealing (GSA) method aimed at finding one of its local minima, which ideally should be the global minimum and for this reason we cannot attribute physical meaning to the adjusted values. However, if an incorrect coordination polyhedron is considered, the values of the Ω_2 and Ω_4 intensity parameters are not well adjusted. In other words, the perfect fit of the theoretical values to the respective Ω_2 and Ω_4 experimental parameters shown in Table 1, confirm that the Sparkle/AM1 modeled structure corresponding to the synthesized structure. In the fitting procedure the response function, F_{resp} , was thus defined as:

$$F_{resp} = \sum_{i=1}^2 \left| \Omega_2^{Calc} - \Omega_2^{Exp} \right| + \left| \Omega_4^{Calc} - \Omega_4^{Exp} \right| \quad (1)$$

where i runs over Sparkle/AM1 geometry, Ω_2^{Calc} and Ω_4^{Calc} were the intensity parameters calculated and Ω_2^{Exp} and Ω_4^{Exp} were the intensity parameters obtained from the experimental emission spectrum.

Aiming at a deeper understanding of the photoluminescence process, the intramolecular energy transfer and back-transfer rates for the Eu(tta)₃ephen complex supported in the MCM matrix were predicted by using the module 3 of LUMPAC. The theoretical model used to describe the ligand-to-Eu³⁺ energy transfer process was developed by Malta and collaborators for lanthanide coordination complexes⁵⁰⁻⁵². According to the model, the energy transfer rates can be inferred from the contributions of the multipolar and exchange mechanisms. The intramolecular energy transfer depends on the distance between the acceptor and the donor states in the energy transfer process (R_L). The R_L values were calculated as 4.84 and 4.99 Å, for $R_L(\text{singlet})$ and $R_L(\text{triplet})$, respectively. According to the selection rules, the ⁵D₂, ⁵L₆, ⁵G₆ and ⁵D₄ levels are good candidates to be involved in the energy transfer processes through the multipolar mechanism⁵², while through the exchange mechanism the ⁵D₁ manifold is the strongest candidate⁸⁸. Moreover, although direct energy transfer to the ⁵D₀ level is not allowed through both processes, this rule is relaxed because of J-mixing effects and thermal population of the ⁷F₁ level⁶⁷. Therefore, we focus our discussion on the multipolar contribution for the ⁵D₄ level (for the ⁵D₂ level the matrix element of the $U^{(2)}$ operator is too small to be taken into account⁸⁸ while the ⁵L₆ and ⁵G₆ levels are not yet included in this LUMPAC version). For the exchange mechanism, the ⁵D₁ and ⁵D₀ levels will be considered (Table 3).

[Table 3]

According to Table 3, the energy transfer rate via the ligand singlet states weakly affects the luminescence process due to its low value ($\sim 10^3 \text{ s}^{-1}$ but with a back-transfer rate almost negligible), compared with the $T_1 \rightarrow ^5D_0$ and $T_1 \leftarrow ^5D_1$ transfer rates ($\sim 10^7 \text{ s}^{-1}$). Accordingly, the most efficient luminescence pathway will be $S_0 \rightarrow S_1 \rightarrow T_1 \rightarrow (^5D_1, ^5D_0) \rightarrow ^7F_{0-6}$. Although the $T_1 \leftarrow ^5D_1$ is quite elevated ($9.18 \times 10^7 \text{ s}^{-1}$), the back transfer rate is also high ($6.09 \times 10^7 \text{ s}^{-1}$),

causing a depopulation of the excited 5D_1 level of the Eu^{3+} ion. Therefore, the dominant pathway is through the $T_1 \rightarrow ^5D_0$ channel ($9.70 \times 10^7 \text{ s}^{-1}$). Additionally, it should be noted that, in resemblance with the F.R.G. e Silva *et al.* work⁸⁸, the $T_1 \leftarrow ^5D_1$ is the direct transfer rate being higher than the $T_1 \rightarrow ^5D_1$.

The theoretical quantitative assessment of energy transfer mechanisms in organic-inorganic hybrids is particularly limited. In fact, up to date, only one report related with a sol-gel derived organic-inorganic di-ureasil hybrid [d-U(600)] incorporating the Eu^{3+} complex $[(\text{Eu}(\text{btfa})_3(4,4'\text{-bpy})(\text{EtOH}))]$ (btfa=benzoyltrifluoroacetate, 4,4'-bpy=4,4'-bipyridine) was performed⁶⁷. The comparison of the calculated values with those obtained for d-U(600)-[Eu(btfa)₃((4,4-bipy)]⁶⁷ shows that the energy transfer rates for the $S_1 \rightarrow ^5D_4$ and $T_1 \rightarrow (^5D_1, ^5D_0)$ channels are approximately 10^4 and 10^3 lower. Although for the d-U(600)-[Eu(btfa)₃((4,4-bipy)] material⁶⁷ the complex was anchored to specific functional groups of the hybrid di-ureasil matrix by the replacement of the ethanol molecule while herein the MCM-41 matrix was used only to support the complex, the observed differences are intrinsically associated with the considered Eu^{3+} β -diketonate complex. In fact, for the isolated $[(\text{Eu}(\text{btfa})_3(4,4'\text{-bpy})(\text{EtOH}))]$ complex, theoretical energy transfer rates of the same order as obtained with the hybrid d-ureasil were found ($\sim 10^7 \text{ s}^{-1}$ for $S_1 \rightarrow ^5D_4$ and $\sim 10^{10} \text{ s}^{-1}$ for $T_1 \rightarrow (^5D_1, ^5D_0)$ channels)²⁰. Similarly, for the isolated $\text{Eu}(\text{tta})_3\text{ephen}$ complex, the $S_1 \rightarrow ^5D_4$ and $T_1 \rightarrow (^5D_1, ^5D_0)$ transfer rates were calculated to be at the same order ($\sim 10^3 \text{ s}^{-1}$ and $\sim 10^7 \text{ s}^{-1}$, unpublished results) of those found for the hybrid MCM-Eu system.

4. Conclusions

Herein, the tris(β -diketonate) $\text{Eu}(\text{tta})_3\text{ephen}$ complex incorporation within the MCM-41 framework was performed and the structural and optical properties of a highly luminescent material is presented and discussed. The combination of UV-Vis and photoluminescence techniques demonstrate the integrity of the first-sphere ligands in the hybrid material suggesting that the structural changes are expected to occur outside the coordination polyhedron, modifying essentially

the second Eu^{3+} coordination shell, most likely by the establishment of intermolecular interactions. For a material that has a simply impregnated lanthanide complex, the herein reported maximum $^5\text{D}_0$ quantum yield (q) value of 0.31 is a significant high value being almost in the same scale of the values obtained for the materials with covalently bonded complexes.

A detailed theoretical photoluminescence study of MCM-Eu performed with the recently developed Luminescence Package- LUMPAC is presented. The high accuracy of the theoretically calculated $^5\text{D}_0$ radiative (k_r) and non-radiative (k_{nr}) transition probabilities as well as the $^5\text{D}_0$ emission quantum efficiency (η) and quantum yield (q) values is achieved through the comparison with the experimental values. Aiming at a deeper understanding of the photoluminescence process, the intramolecular energy transfer and back -transfer rates were also predicted. The $\text{S}_0 \rightarrow \text{S}_1 \rightarrow \text{T}_1 \rightarrow ^5\text{D}_0 \rightarrow ^7\text{F}_{0-6}$ channel was found to be dominant pathway with a $\text{T}_1 \rightarrow ^5\text{D}_0$ rate of $9.70 \times 10^7 \text{ s}^{-1}$.

The good agreement found between theoretical and experimental values provides a further support to the theoretical scheme that has been herein proposed for the modelling of the MCM-based lanthanide materials. In fact, this work addresses the challenge of building a theoretical methodology, through the LUMPAC, for modelling the luminescence properties of extended solids. This is a necessary step that must be taken in the near future for opening the way to a rational design of such materials.

Acknowledgments

The authors are grateful to FCT, COMPETE and FEDER programs (Pest-C/CTM/LA0011/2013, Pest-C/CTM/LA0025/2013, PEst-OE/QUI/UI0612/2013, PEst-OE/QUI/UI0100/2013). QREN is thanked for a grant to M.M.N under the project CENTRO-07-ST24-FEDER-002032 (grant number BPD/UI96/3340/2014). The Brazilian author appreciates the financial support from the Brazilian agencies, institutes and networks: CNPq, INAMI and FAPITEC-SE.

Supporting Information Available

Figures S1-S2. This material is available free of charge via the Internet at <http://pubs.rsc.org>.

References

- 1 E. G. Moore, A. P. S. Samuel and K. N. Raymond, *Accounts Chem. Res.*, 2009, **42**, 542-552.
- 2 S. V. Eliseeva and J. -C. G. Bünzli, *Chem. Soc. Rev.*, 2010, **39**, 189-227.
- 3 L. Armelao, S. Quici, F. Barigelletti, G. Accorsi, G. Bottaro, M. Cavazzini and E. Tondello, *Coord. Chem. Rev.*, 2010, **254**, 487-505.
- 4 L. D. Carlos, R. A. S. Ferreira, V. de Zea Bermudez, B. Julian-Lopez and P. Escribano, *Chem. Soc. Rev.*, 2011, **40**, 536-549.
- 5 A. Polman and F. van Veggel, *J. Opt. Soc. Am. B-Opt. Phys.*, 2004, **21**, 871-892.
- 6 W. Quirino, R. Reyes, C. Legnani, P. C. Nobrega, P. A. Santa-Cruz and M. Cremona, *Synth. Met.*, 2011, **161**, 964-968.
- 7 A. Q. L. Quang, V. G. Truong, A. M. Jurdyc, B. Jacquier, J. Zyss and I. Ledoux, *J. Appl. Phys.*, 2007, **101**, 023110.
- 8 L. J. Charbonniere, N. Hildebrandt, R. F. Ziessel and H. G. Loehmannsroeben, *J. Am. Chem. Soc.*, 2006, **128**, 12800-12809.
- 9 T. X. Wang, J. Zhang, W. Ma, Y. H. Luo, L. J. Wang, Z. J. Hu, W. X. Wu, X. Wang, G. Zou and Q. J. Zhang, *Sol. Energy*, 2011, **85**, 2571-2579.
- 10 C. D. S. Brites, P. P. Lima, N. J. O. Silva, A. Millan, V. S. Amaral, F. Palacio and L. D. Carlos, *Adv. Mater.*, 2010, **22**, 4499-4504.
- 11 M. P. Placidi, J. Engelmann, L. S. Natrajan, N. K. Logothetis and G. Angelovski, *Chem. Commun.*, 2011, **47**, 11534-11536.
- 12 G. F. de Sa, O. L. Malta, C. D. Donega, A. M. Simas, R. L. Longo, P. A. Santa-Cruz and E. F. da Silva, *Coord. Chem. Rev.*, 2000, **196**, 165-195.
- 13 K. Binnemans, in *Rare Earth Beta-Diketonates*, Elsevier, Amsterdam, 2005.
- 14 M. M. Nolasco, P. M. Vaz, V. T. Freitas, P. P. Lima, P. S. André, R. A. S. Ferreira, P. D. Vaz, P. Ribeiro-Claro and L. D. Carlos, *J. Mater. Chem. A*, 2013, **1**, 7339-7350.
- 15 J. A. Kai, M. Felinto, L. A. O. Nunes, O. L. Malta and H. F. Brito, *J. Mater. Chem.*, 2011, **21**, 3796-3802.

- 16 J. B. Yu, L. N. Sun, H. S. Peng and M. I. J. Stich, *J. Mater. Chem.*, 2010, **20**, 6975-6981.
- 17 K. Binnemans, *J. Mater. Chem.*, 2009, **19**, 448-453.
- 18 P. P. Lima, F. A. A. Paz, R. A. S. Ferreira, V. de Zea Bermudez and L. D. Carlos, *Chem. Mater.*, 2009, **21**, 5099-5111.
- 19 L. D. Carlos, R. A. S. Ferreira, V. de Zea Bermudez and S. J. L. Ribeiro, *Adv. Mater.*, 2009, **21**, 509-534.
- 20 P. P. Lima, R. A. S. Ferreira, R. O. Freire, F. A. A. Paz, L. S. Fu, S. Alves, L. D. Carlos and O. L. Malta, *ChemPhysChem*, 2006, **7**, 735-746.
- 21 T. Fukuda, S. Yamauchi, Z. Honda, N. Kamata and N. Kijima, *Phys. Status Solidi RRL*, 2009, **3**, 296-98.
- 22 X. M. Guo, J. L. Canet, D. Boyer, P. Adumeau and R. Mahiou, *J. Sol-Gel Sci. Technol.*, 2012, **64**, 404-410.
- 23 B. Yan, *RSC Adv.*, 2012, **2**, 9304-9324.
- 24 J. Feng and H. J. Zhang, *Chem. Soc. Rev.*, 2013, **42**, 387-410.
- 25 Y. X. Ding, Y. G. Wang, H. R. Li, Z. Y. Duan, H. H. Zhang and Y. X. Zheng, *J. Mater. Chem.*, 2011, **21**, 14755-14759.
- 26 Q. H. Xu, L. S. Li, X. S. Liu and R. R. Xu, *Chem. Mater.*, 2002, **14**, 549-555.
- 27 S. W. Li, H. W. Song, W. L. Li, X. G. Ren, S. Z. Lu, G. H. Pan, L. B. Fan, H. Q. Yu, H. Zhang, R. F. Qin, Q. L. Dai and T. Wang, *J. Phys. Chem. B*, 2006, **110**, 23164-23169.
- 28 H. Zhang, Y. Xu, W. Yang and Q. G. Li, *Chem. Mater.*, 2007, **19**, 5875-5881.
- 29 C. Zhao, L. Y. Feng, B. L. Xu, J. S. Ren and X. G. Qu, *Chem. Eur. J.*, 2011, **17**, 7007-7012.
- 30 L. Maggini, F. M. Toma, L. Feruglio, J. M. Malicka, T. Da Ros, N. Armaroli, M. Prato and D. Bonifazi, *Chem. Eur. J.*, 2012, **18**, 5889-5897.
- 31 K. Binnemans, *Chem. Rev.*, 2009, **109**, 4283-4374.
- 32 W. H. Zhang, J. L. Shi, L. Z. Wang and D. S. Yan, *Chem. Mater.*, 2000, **12**, 1408-1413.
- 33 J. Yu, J. L. Shi, L. Z. Wang, M. L. Ruan and D. S. Yan, *Mater. Lett.*, 2001, **48**, 112-116.

- 34 T. Maschmeyer, F. Rey, G. Sankar and J. M. Thomas, *Nature*, 1995, **378**, 159-162.
- 35 R. Burch, N. Cruise, D. Gleeson and S. C. Tsang, *Chem. Commun.*, 1996, 951-952.
- 36 Y. Li and B. Yan, *J. Fluoresc.*, 2009, **19**, 191-201.
- 37 C. Peng, H. Zhang, J. Yu, Q. Meng, L. Fu, H. Li, L. Sun and X. Guo, *J. Phys. Chem. B.*, 2005, **109**, 15278-15287.
- 38 S. Gago, J. A. Fernandes, J. P. Rainho, R. A. S. Ferreira, M. Pillinger, A. A. Valente, T. M. Santos, L. D. Carlos, P. J. A. Ribeiro-Claro and I. S. Gonçalves, *Chem. Mater.*, 2005, **17**, 5077-5084.
- 39 S. M. Bruno, R. A. S. Ferreira, F. A. Almeida Paz, L. D. Carlos, M. Pillinger, P. Ribeiro-Claro and I. S. Gonçalves, *Inorg. Chem.*, 2009, **48**, 4882-4895.
- 40 Q. G. Meng, P. Boutinaud, A.-C. Franville, H. J. Zhang and R. Mahiou, *Microporous Mesoporous Mater.*, 2003, **65**, 127-136.
- 41 A. Fernandes, J. Dexpert-Ghys, A. Gleizes, A. Galarneau and D. Brunel, *Microporous Mesoporous Mater.*, 2005, **83**, 35-46.
- 42 L. C. Cides da Silva, T. S. Martins, M. Santos Filho, E. E. S. Teotônio, P. C. Isolani, H. F. Brito, M. H. Tabacniks, M. C. A. Fantini and J. R. Matos, *Microporous Mesoporous Mater.*, 2006, **92**, 94-100.
- 43 Y. Li, B. Yan and H. Yang, *J. Phys. Chem. C*, 2008, **112**, 3959-3968.
- 44 S. M. Bruno, R. A. S. Ferreira, L. D. Carlos, M. Pillinger, P. Ribeiro-Claro and I. S. Gonçalves, *Microporous Mesoporous Mater.*, 2008, **113**, 453-462.
- 45 Q. Xu, L. Li, X. Liu and R. Xu, *Chem Mater.*, 2002, **14**, 549-555.
- 46 C. D. Nunes, A. A. Valente, M. Pillinger, A. C. Fernandes, C. C. Romão, J. Rocha and I. S. Gonçalves, *J. Mater. Chem.*, 2002, **12**, 1735-1742.
- 47 A. V. M. de Andrade, N. B. da Costa Jr., R. L. Longo, O. L. Malta, A. M. Simas and G. F. de Sá, *Mol. Eng.*, 1997, **7**, 293-308.

- 48 O. L. Malta, H. F. Brito, J. F. S. Menezes, F. R. Gonçalves e Silva, S. Alves Jr., F. S. Farias Jr. and A. V. M. de Andrade, *J. Lumin.*, 1997, **75**, 255-347.
- 49 H. J. Batista, A. V. M de Andrade, R. L. Longo, A. M. Simas, G. F. de Sá, N. K. Ito and L. C. Thompson, *Inorg. Chem.*, 1998, **37**, 3542-3547.
- 50 F. R. G. E. Silva and O. J. Malta, *J. Alloys and Compd.*, 1997, **250**, 427-430.
- 51 O. J. Malta, *J. Lumin.*, 1997, **71**, 229-230.
- 52 O. J. Malta, *J. Non-Cryst. Solids*, 2008, **354**, 4770-4776.
- 53 O. L. Malta, H. F. Brito, J. F. S. Menezes, F. R. Gonçalves e Silva, C. de Mello Donegá and S. Alves Jr., *Chem. Phys. Lett.*, 1998, **282**, 233-238.
- 54 J. D. L. Dutra, T. P. Bispo and R. O. Freire, *J. Comput. Chem.*, 2014, **35**, 772-775.
- 55: M. Nolasco, R. Mendes; P. Lima; F. Paz; L. D. Carlos and J. Rocha, *Eur. J. Inorg. Chem.*, 2014, DOI: 10.1002/ejic.201402492.
- 56 N. U. Silva, C. I. Fernandes, T. G. Nunes, M. S. Saraiva, C. D. Nunes and P. D. Vaz, *Applied Catal. A: Gen.*, 2011, **408**, 105-116.
- 57 <http://boba.boom.ru/eng/mcm-41.html>, accessed on 8 April 2005.
- 58 P. Ugliengo, D. Viterbo and G. Chiari, *Zeitschrift für Kristallographie*, 1993, **207**, 9-23.
- 59 M. J. Frisch, G. W. Trucks, H. B. Schlegel, G. E. Scuseria, M. A. Robb, J. R. Cheeseman, J. A. Montgomery, Jr., T. Vreven, K. N. Kudin, J. C. Burant, J. M. Millam, S. S. Iyengar, J. Tomasi, V. Barone, B. Mennucci, M. Cossi, G. Scalmani, N. Rega, G. A. Petersson, H. Nakatsuji, M. Hada, M. Ehara, K. Toyota, R. Fukuda, J. Hasegawa, M. Ishida, T. Nakajima, Y. Honda, O. Kitao, H. Nakai, M. Klene, X. Li, J. E. Knox, H. P. Hratchian, J. B. Cross, V. Bakken, C. Adamo, J. Jaramillo, R. Gomperts, R. E. Stratmann, O. Yazyev, A. J. Austin, R. Cammi, C. Pomelli, J. W. Ochterski, P. Y. Ayala, K. Morokuma, G. A. Voth, P. Salvador, J. J. Dannenberg, V. G. Zakrzewski, S. Dapprich, A. D. Daniels, M. C. Strain, O. Farkas, D. K. Malick, A. D. Rabuck, K. Raghavachari, J. B. Foresman, J. V. Ortiz, Q. Cui, A. G. Baboul, S. Clifford, J. Cioslowski, B. B. Stefanov, G. Liu, A. Liashenko, P. Piskorz, I. Komaromi, R. L. Martin, D. J. Fox, T. Keith, M. A.

- Al-Laham, C. Y. Peng, A. Nanayakkara, M. Challacombe, P. M. W. Gill, B. Johnson, W. Chen, M. W. Wong, C. Gonzalez, and J. A. Pople, Gaussian, Inc., Wallingford CT, 2004.
- 60 R. O. Freire, G. B. Rocha and A. M. Simas, *Inorg. Chem.*, 2005, **44**, 3299-3310.
- 61 R. O. Freire and A. M. Simas, *J. Chem. Theory Comput.*, 2010, **6**, 2019-2023.
- 62 R. O. Freire, G. B. Rocha and A. M. Simas, *J. Braz. Chem. Soc.*, 2009, **20**, 1638-1645.
- 63 M. A. M. Filho, J. D. L. Dutra, G. B. Rocha, R. O. Freire and A. M. Simas, *R. Soc. Chem. Adv.*, 2013, **3**, 16747-16755.
- 64 J. D. L. Dutra, M. A. M. Filho, G. B. Rocha, R. O. Freire, A. M. Simas and J. J. P. Stewart, *J. Chem. Theory. Comput.*, 2013, **9**, 3333-3341.
- 65 J. P. Stewart, MOPAC2012, Stewart Computational Chemistry, Version 13.113W; Colorado Springs: CO, USA, 2012.
- 66 R. O. Freire, G. B. Rocha and A. M. Simas, *J. Mol. Model.*, 2006, **12**, 373-389.
- 67 P. P. Lima, S. S. Nobre, R. O. Freire, S. A. Júnior, R. A. S. Ferreira, U. Pischel, O. L. Malta and L. D. Carlos, *J. Phys. Chem. C*, 2007, **111**, 17627-17634.
- 68 J. E. Ridley and M. C. Zerner, *Theor. Chim. Acta*, 1976, **42**, 223-239.
- 69 M. C. Zerner, G. H. Loew and R. F. Kirchner, *J. Am. Chem. Soc.*, 1980, **102**, 589-599.
- 70 F. Nesse, *WIREs Comput. Mol. Sci.*, 2012, **2**, 73-78.
- 71 J. D. L. Dutra and R. O. Freire, *J. Photochem. Photobiol. A*, 2013, **256**, 29-35.
- 72 B. Marler, U. Oberhagemann, S. Voltmann and H. Gies, *Microporous Mesoporous Mater.*, 1996, **6**, 375-383.
- 73 W. Hammond, E. Prouzet, S. D. Mahanti and T. J. Pinnavaia, *Microporous Mesoporous Mater.*, 1999, **27**, 19-25.
- 74 S. J. Gregg, K. S. W. Sing, *Adsorption, Surface Area and Porosity*, 2nd Ed., Academic Press, London, 1982.
- 75 P. D. Vaz, C. D. Nunes, M. Vasconcellos-Dias, M. M. Nolasco, P. J. A. Ribeiro Claro and M. J. Calhorda, *Chem. Eur. J.*, 2007, **13**, 7874-7882.

- 76 X. Guo, L. Fu, H. Zhang, L. D. Carlos, C. Peng, J. Guo, J. Yu, R. Deng and L. Sun, *New J. Chem.*, 2005, **29**, 1351-1358.
- 77 N. Petkova, S. Gutzov, N. Lesev, S. Kaloyanova, S. Stoyanov and T. Deligeorgiev, *Optical Materials*, 2011, **33**, 1715–1720.
- 78 N. Danchovo, S. Gutzov, K. Matras-Postolek, M. Bredol, N. Lesev, S. Kaloyanova and T. Deligeorgiev, *J. Incl. Phenom. Macrocycl. Chem.*, 2014, **78**, 381–386.
- 79 R. A. S. Ferreira, M. Nolasco, A. C. Roma, R. L. Longo, O. L. Malta and L. D. Carlos, *Chem. Eur. J.*, 2012, **18**, 12130-12139.
- 80 M. Fernandes, V. de Zea Bermudez, R. A. S. Ferreira, L. D. Carlos, A. Charas, J. Morgado, M. M. Silva and M. J. Smith, *Chem. Mater.*, 2007, **19**, 3892-3901.
- 81 C-V. Kumar and Z. J. Williams, *J. Phys. Chem. C*, 1995, **99**, 17632-17639.
- 82 W. T. Carnall, H. Crosswhite and H. M. Crosswhite, *Energy Level Structure and Transition Probabilities of the Trivalent Lanthanides in LaF₃*, Argonne Laboratory Report, Illinois, 1977.
- 83 F. R. G. e Silva, J. F. S. Menezes, G. B. Rocha, S. Alves, H. F. Brito, R. L. Longo and O. L. Malta, *J. Alloy Compd.*, 2000, **303-304**, 364-370.
- 84 X. Li, Z. Wu, Z. Si, L. Zhou, X. Liu and H. Zhang, *Phys. Chem. Chem. Phys.*, 2009, **11**, 9687-9695.
- 85 M. Shi, F. Li, T. Yi, D. Zhang, H. Hu and C. Huang, *Inorg. Chem.*, 2005, **44**, 8929-8936.
- 86 M. F. Belian, H. J. Batista, A. G. S. Bezerra, W. E. Silva, G. F. de Sá and S. Alves Jr., *J. Chem. Phys.*, 2011, **381**, 29-34.
- 87 H. Xu and W. Huang, *J. Photoch. Photobio. A*, 2011, **217**, 205-213.
- 88 O. L. Malta and F.R.G.E. Silva, *Spectrochim. Acta Part A*, 1998, **54**, 1593-1599.

Figures and Tables captions

Table 1- Charge factors (g) and polarizabilities (α) for the hybrid **MCM-Eu** system; (1) refers to the oxygen atoms that belong to one side of the tta ligand with thenoyl group; (2) to the oxygen atoms that belong to one side of the tta ligand with CF_3 group and (3) to the nitrogen from the ephen ligand.

Table 2- Experimental (obtained with excitation wavelength of 375 nm) and theoretical values of intensity parameters (Ω), radiative (k_r) and non-radiative (k_{nr}) transition probabilities and emission quantum efficiency (η) and quantum yield (q) values of the $^5\text{D}_0$ emitting level calculated for the hybrid MCM-Eu system.

Table 3- Theoretical values of intramolecular energy transfer and back –transfer rates (s^{-1}) calculated for the hybrid MCM-Eu system.

Scheme 1. Impregnation procedure for immobilization of the $\text{Eu}(\text{tta})_3\text{ephen}$ complex inside MCM-41 pores.

Figure 1. X-ray diffraction (XRD) powder patterns of mesoporous materials MCM and **MCM-Eu**.

Figure 2. Thermogravimetric analyses (TGA) profiles of MCM and **MCM-Eu**.

Figure 3. ^{29}Si CP MAS-DD spectra of MCM (bottom) and **MCM-Eu** (top).

Figure 4. Normalised diffuse reflectance infrared Fourier transform (DRIFT) spectra of $\text{Eu}(\text{tta})_3\text{ephen}$ (black line), MCM matrix (blue line) and the **MCM-Eu** sample (red line)

Figure 5. Ultraviolet-Visible (UV-Vis) absorption spectra of Euttaephen (black line) and the **MCM-Eu** sample (red line) in ethanolic solutions.

Figure 6. Room-temperature emission (PL) and excitation (PLE) spectra of the **MCM-Eu** sample excited at 375 nm and monitored at 612 nm, respectively. The inset shows a magnification of the $^7\text{F}_0 \rightarrow ^5\text{D}_2$ transition.

Figure 7. (a) 10 K intra-4f⁶ high-resolution emission spectra of **MCM-Eu** at (1) 275 nm and (2) 375 nm. (b) Magnification of the ${}^7F_0 \rightarrow {}^5D_0$ transition. The solid lines correspond to the data best fit using a single Gaussian function ($R > 0.98$). (c) Residual plot resulting from the fit procedure.

Figure 8. Partial schematic representation of the ground state geometry of the hybrid **MCM-Eu** system calculated by the Sparkle/AM1 model showing the establishment of different C-H...O intermolecular interactions (calculated intermolecular H...O distances in Å).

Table 1

MCM-Eu	Intensity parameters (10^{-20} cm ²)			k_r (s ⁻¹)	k_{nr} (s ⁻¹)	η (%)	q (%)
	Ω_2	Ω_4	Ω_6				
Experimental	15.76	7.38	630	860	42	26
Theoretical	15.76	7.38	0.18	638	853	43	35

Table 2

MCM-Eu	Charge factor			Polarizability (\AA^3)		
	g(1)	g(2)	g(3)	$\alpha(1)$	$\alpha(2)$	$\alpha(3)$
Theoretical	0.4319	0.1111	0.1809	3.2901	5.9361	6.0074

Table 3

MCM-Eu	Transfer rate (s ⁻¹)	Back-transfer rate (s ⁻¹)
$S_1 \rightarrow {}^5D_4$	5.97×10^3 (*)	8.98×10^{-10} (*)
$T_1 \leftarrow {}^5D_1$	9.18×10^7	6.09×10^7
$T_1 \rightarrow {}^5D_0$	9.70×10^7	2.95×10^4

(*) multipolar mechanism

Figure 1

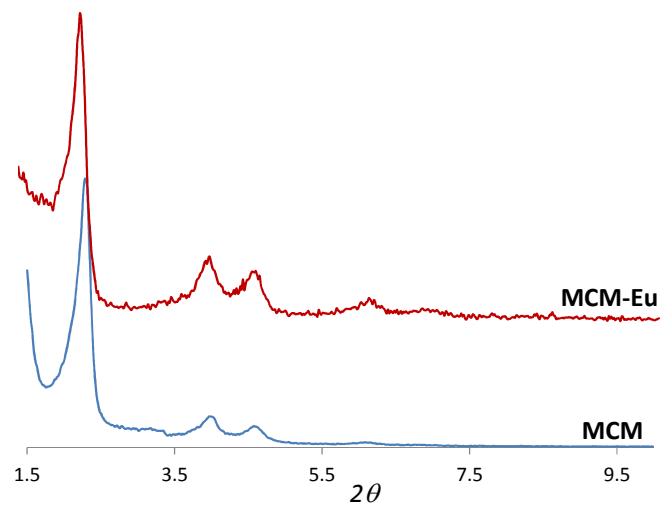


Figure 2

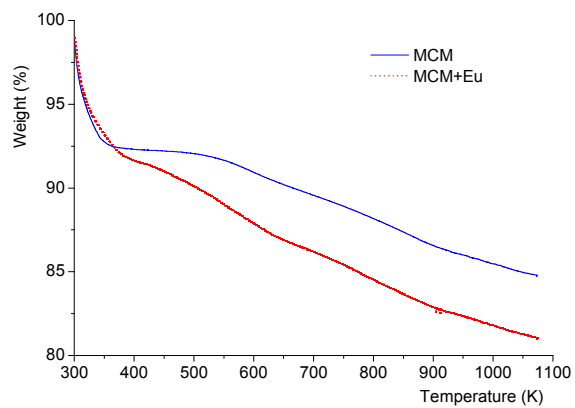


Figure 3

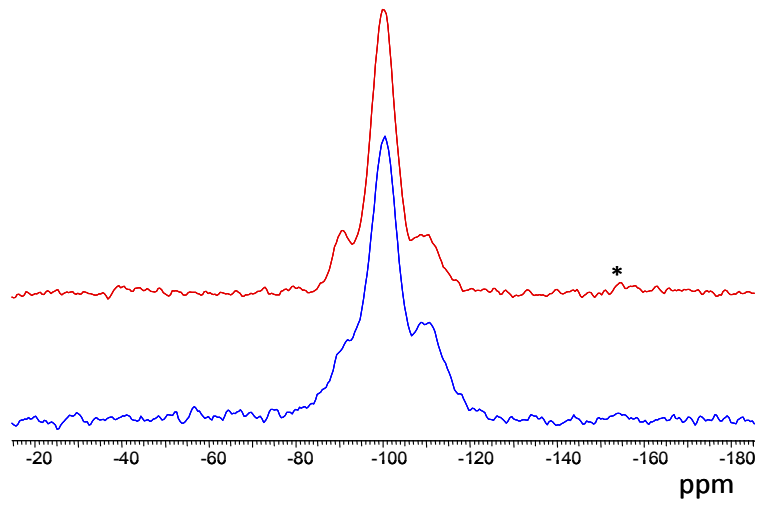


Figure 4

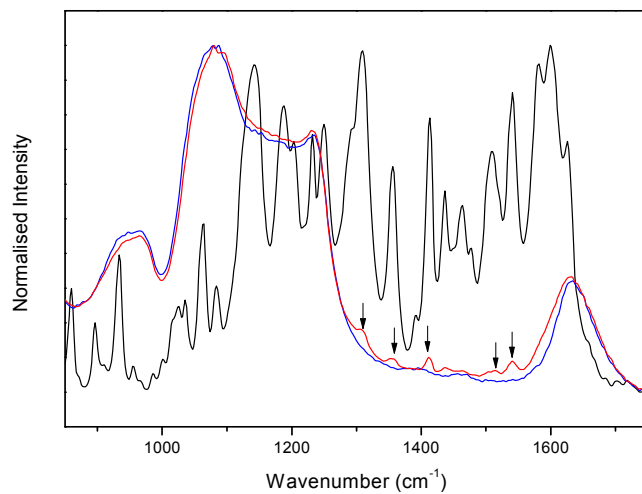


Figure 5

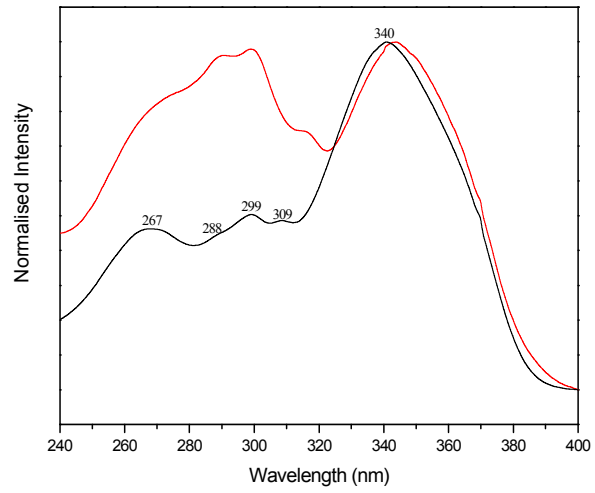


Figure 6

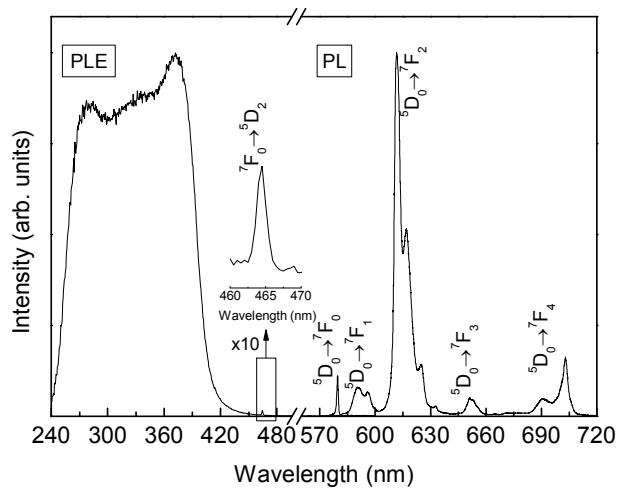


Figure 7

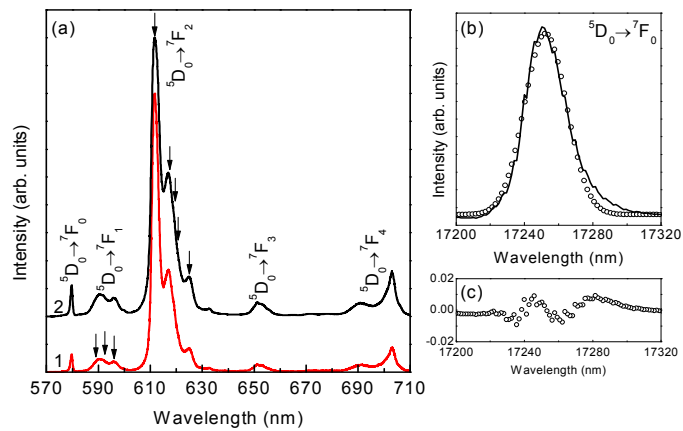
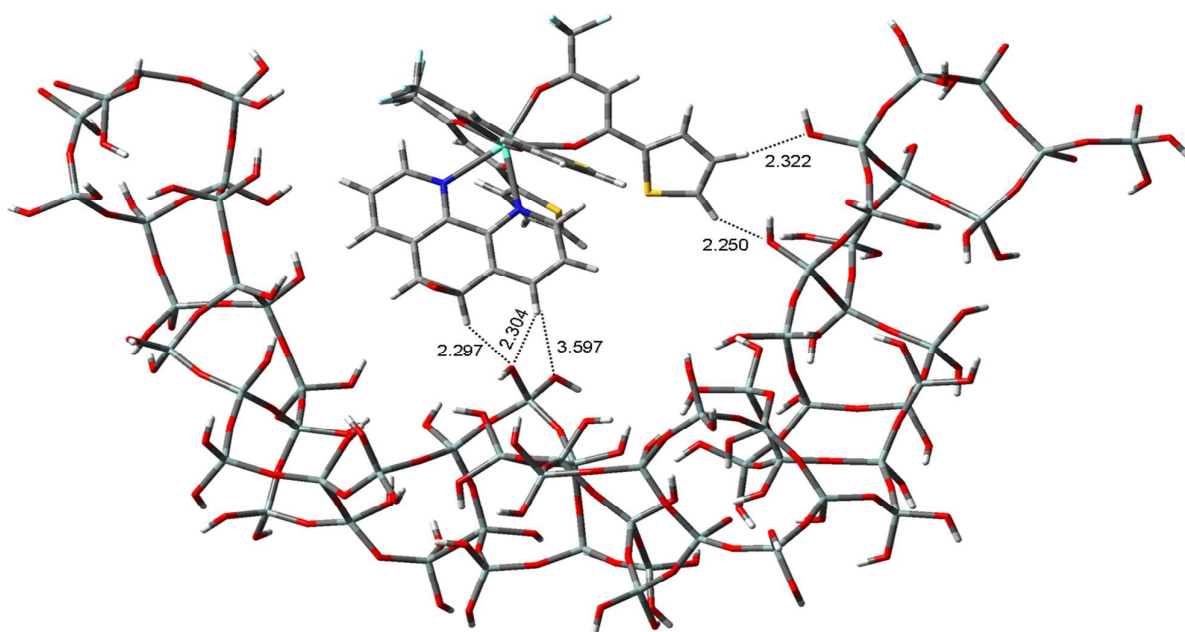
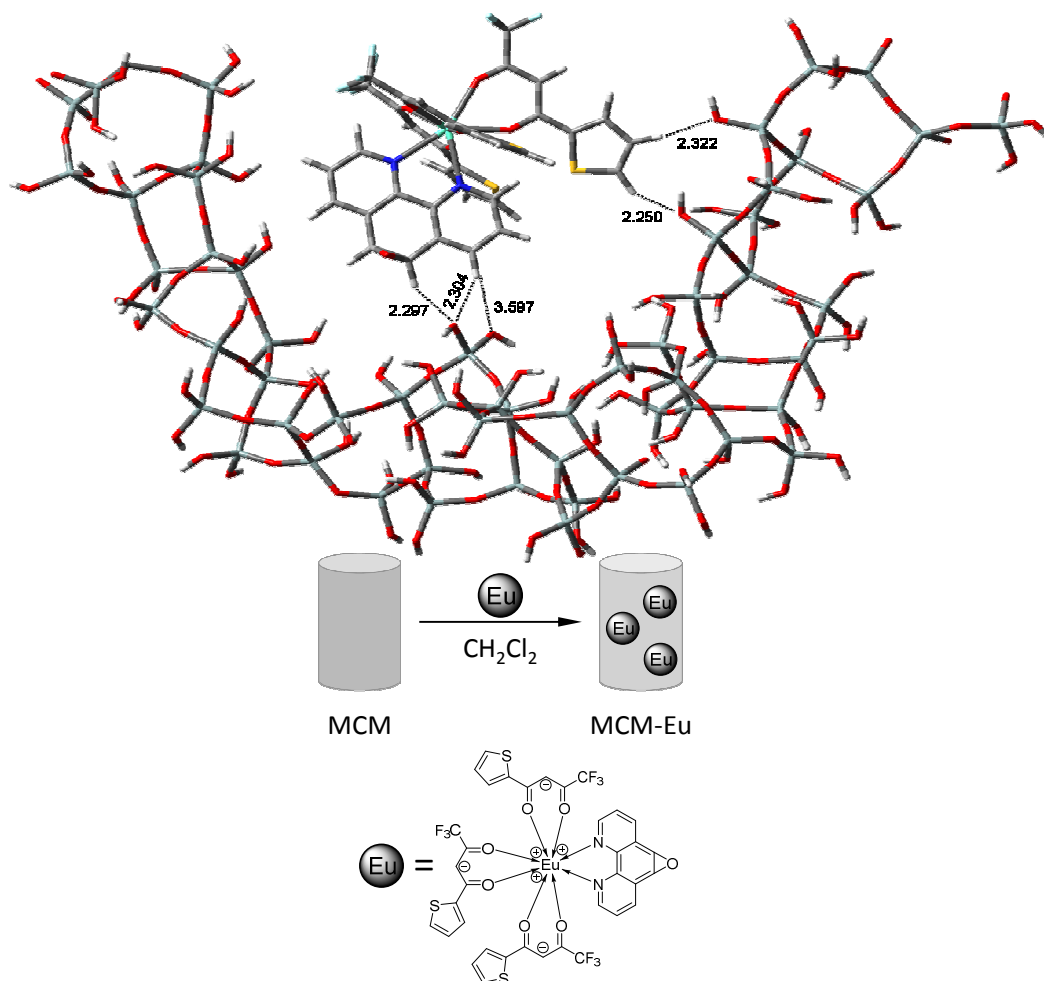


Figure 8



Graphical abstract



The mesoporous silica MCM-41 was used as a support for the incorporation of the highly luminescent tris(β -diketonate) complex $\text{Eu}(\text{tta})_3\text{ephen}$ yielding the hybrid MCM-Eu material. Aiming at a deeper understanding of the photoluminescence process, a detailed theoretical photoluminescence study of the MCM-Eu with the recently developed Luminescence Package-LUMPAC is presented and the ligand-to- Eu^{3+} intramolecular energy transfer and back-transfer rates predicted. The dominant pathway involves the energy transfer between the lowest energy ligand triplet and the $^5\text{D}_0$ level ($9.70 \times 10^7 \text{ s}^{-1}$).